produce analogs of **2** differing in the alcohol functionalities (C-3, C-4, C-5, and C-20) to better understand the structure-activity relationship of ingenanes.

The synthesis of ingenol (**1**) presented herein illustrates the power of two-phase logic to deliver an efficient, concise synthesis even in architecturally complex settings. The usefulness of the two-phase approach will undoubtedly continue to expand as new methods for C–C bond formation and C–H oxidation are developed. Furthermore, this report provides a strong rebuttal to the presumption that chemical synthesis is ill-equipped to deal with the preparation of structurally complex terpenoid drug molecules. Rather, in this instance, total chemical synthesis holds promise as the best method to both prepare ingenol mebutate (**2**) and enable the development of therapeutic analogs with broader utility in the treatment of human diseases.

References and Notes

1. F. E. Koehn, G. T. Carter, *Nat. Rev. Drug Discov.* **4**, 206–220 (2005).
2. I. Raskin *et al.*, *Trends Biotechnol.* **20**, 522–531 (2002).
3. P. G. Mountford, in *Green Chemistry in the Pharmaceutical Industry*, P. J. Dunn, A. S. Wells, M. T. Williams, Eds. (Wiley, Weinheim, Germany, 2010), pp. 145–160.
4. C. J. Paddon *et al.*, *Nature* **496**, 528–532 (2013).
5. C. Zhu, S. P. Cook, *J. Am. Chem. Soc.* **134**, 13577–13579 (2012).
6. J. D. Keasling, A. Mendoza, P. S. Baran, *Nature* **492**, 188–189 (2012).
7. J. D. Keasling, *Science* **330**, 1355–1358 (2010).
8. E. Hecker, *Cancer Res.* **28**, 2338–2349 (1968).
9. K. Zechmeister *et al.*, *Tetrahedron Lett.* **11**, 4075–4078 (1970).
10. R. W. Alder, S. P. East, *Chem. Rev.* **96**, 2097–2112 (1996).
11. S. M. Ogbourne *et al.*, *Cancer Res.* **64**, 2833–2839 (2004).
12. M. Fujiwara *et al.*, *Antimicrob. Agents Chemother.* **40**, 271–273 (1996).
13. A. Vasas, D. Rédei, D. Csupor, J. Molnár, J. Hohmann, *Eur. J. Org. Chem.* **2012**, 5115–5130 (2012).
14. C. M. Hasler, G. Acs, P. M. Blumberg, *Cancer Res.* **52**, 202–208 (1992).
15. U.S. Food and Drug Administration, *2012 Novel New Drugs Summary* (FDA, Washington, DC, 2013); www.fda.gov/downloads/Drugs/DevelopmentApprovalProcess/DrugInnovation/UCM337830.pdf.
16. G. Siller *et al.*, *Australas. J. Dermatol.* **51**, 99–105 (2010).
17. "European public assessment report: Picato" [European Medicines Agency (EMA) publication 650464, London, 2012]; www.ema.europa.eu/docs/en_GB/document_library/EPAR_-_Public_assessment_report/human/002275/WC500135329.pdf.
18. X. Liang, G. Grue-Sørensen, A. K. Petersen, T. Högberg, *Synlett* **23**, 2647–2652 (2012).
19. J. Hohmann, F. Evanics, L. Berta, T. Bartók, *Planta Med.* **66**, 291–294 (2000).
20. G. Appendino, G. C. Tron, G. Cravotto, G. Palmisano, J. Jakupovic, *J. Nat. Prod.* **62**, 76–79 (1999).
21. V. Hale, J. D. Keasling, N. Renninger, T. T. Diagana, *Am. J. Trop. Med. Hyg.* **77** (suppl.), 198–202 (2007).
22. R. J. Schmidt, *J. Linn. Soc. Bot.* **94**, 221–230 (1987).
23. J. Kirby *et al.*, *Phytochemistry* **71**, 1466–1473 (2010).
24. I. Kuwajima, K. Tanino, *Chem. Rev.* **105**, 4661–4670 (2005).
25. J. D. Winkler, M. B. Rouse, M. F. Greaney, S. J. Harrison, Y. T. Jeon, *J. Am. Chem. Soc.* **124**, 9726–9728 (2002).
26. K. Tanino *et al.*, *J. Am. Chem. Soc.* **125**, 1498–1500 (2003).
27. A. Nickel *et al.*, *J. Am. Chem. Soc.* **126**, 16300–16301 (2004).
28. K. Watanabe *et al.*, *J. Org. Chem.* **69**, 7802–7808 (2004).
29. O. L. Epstein, J. K. Cha, *Angew. Chem. Int. Ed.* **44**, 121–123 (2004).
30. G. Appendino *et al.*, *Eur. J. Org. Chem.* **1999**, 3413–3420 (1999).
31. K. Chen, P. S. Baran, *Nature* **459**, 824–828 (2009).
32. A. Nakamura, M. Nakada, *Synthesis* **45**, 1421–1451 (2013).
33. T. Konegawa, Y. Ohtsuka, H. Ikeda, T. Sugai, H. Ohta, *Synlett* **1997**, 1297–1299 (1997).
34. K. M. Brummond *et al.*, *Org. Lett.* **4**, 1931–1934 (2002).
35. K. Shibuya, *Synth. Commun.* **24**, 2923–2941 (1994).
36. P. A. Wender, V. A. Verma, T. J. Paxton, T. H. Pillow, *Acc. Chem. Res.* **41**, 40–49 (2008).
37. N. Z. Burns, P. S. Baran, R. W. Hoffmann, *Angew. Chem. Int. Ed.* **48**, 2854–2867 (2009).

Mapping of Functional Groups in Metal-Organic Frameworks

Xueqian Kong,[1,2]* Hexiang Deng,[3,4]*† Fangyong Yan,[1,4]* Jihan Kim,[4]‡ Joseph A. Swisher,[1,4] Berend Smit,[1,3,4] Omar M. Yaghi,[3,4,5]§ Jeffrey A. Reimer[1,2]§

We determined the heterogeneous mesoscale spatial apportionment of functional groups in a series of multivariate metal-organic frameworks (MTV-MOF-5) containing BDC (1,4-benzenedicarboxylate) linkers with different functional groups—B (BDC-NH2), E (BDC-NO2), F [(BDC-(CH3)2], H [BDC-(OC3H5)2], and I [BDC-(OC7H7)2]—using solid-state nuclear magnetic resonance measurements combined with molecular simulations. Our analysis reveals that these methods discern between random (EF), alternating (EI and EHI), and various cluster (BF) forms of functional group apportionments. This combined synthetic, characterization, and computational approach predicts the adsorptive properties of crystalline MTV-MOF systems. This methodology, developed in the context of ordered frameworks, is a first step in resolving the more general problem of spatial disorder in other ordered materials, including mesoporous materials, functionalized polymers, and defect distributions within crystalline solids.

A strategy for optimizing the properties of synthetic crystalline materials is to deliberately introduce heterogeneity by increasing the number of constituents (*1*). This approach can be compromised by the dual challenges of phase separation, lack of order, or both. Multivariate metal-organic frameworks (MTV-MOFs) can meet this challenge by incorporating multiple linkers that bear different functional groups into the same crystal, which creates a heterogeneous interior (*2*). This heterogeneity can enhanced selectivity for carbon dioxide (CO_2) capture and hydrogen uptake relative to mixtures of pure materials. On a fundamental level, these materials present characterization challenges, in that there are no experimental techniques that can elucidate the intermingling of functional groups that characterizes the heterogeneity within the crystalline MTV-MOFs. For example, this "heterogeneity problem" is intractable for diffraction methods (x-ray, neutron, and electron) and remains unexamined with other characterization methods. We show that multidimensional solid-state nuclear magnetic resonance (SSNMR) combined with molecular simulations can be used to generate three-dimensional (3D) maps of the apportionment of functional groups (Fig. 1) within and between the pores of MTV-MOF-5. These MTV-MOFs adopt MOF-5 structure containing BDC (1,4-benzenedicarboxylate) linkers with different functional groups–B (BDC-NH2), E (BDC-NO2), F [(BDC-(CH3)2], H [BDC-(OC3H5)2], and I [BDC-(OC7H7)2]—using solid-state nuclear magnetic resonance measurements combined with molecular simulations. This method can be applied to other ordered or disordered systems to

[1]Department of Chemical and Biomolecular Engineering, University of California, Berkeley, CA 94720, USA. [2]Environmental Energy Technologies Division, Lawrence Berkeley National Laboratory, Berkeley, CA 94720, USA. [3]Department of Chemistry, University of California, Berkeley, CA 94720, USA. [4]Materials Sciences Division, Lawrence Berkeley National Laboratory, Berkeley, CA 94720, USA. [5]NanoCentury KAIST Institute and Graduate School of Energy, Environment, Water, and Sustainability (World Class University), Daejeon 305-701, Republic of Korea.

*These authors contributed equally to this work.
†Present address: College of Chemistry and Molecular Sciences, Wuhan University Luojiashan, Wuhan, 430072 China.
‡Present address: Department of Chemical and Biomolecular Engineering, Korea Advanced Institute of Science and Technology, 291 Daehak-ro Yuseong-gu, Daejeon, 305-701 Korea.
§Corresponding author. E-mail: yaghi@berkeley.edu (O.M.Y.); reimer@berkeley.edu (J.A.R.)

map the distributions of functional groups, ligands, particles, or defects.

Our analysis indicates that, depending on the combination of various kinds of functionality and their ratios, three distinct apportionments of those functionalities exist: random, alternating, and clustered. Upon discerning these apportionments, we can then predict and explain (i) the CO_2 adsorption isotherm and the observed differences in selectivity, (ii) the changes in apportionment of functionalities as a function of composition and functionality ratio, and (iii) the apportionment in ternary functionality mixtures based on their binary NMR data.

Different interactions between linkers can lead to different apportionment scenarios. Linkers with preferential interactions with each other form clusters, whereas linkers with preferential interactions with different linkers lead to alternating structures. Linkers with no preferences give a random structure. The SSNMR distance measurements represent an average of pairwise interactions throughout the entire sample and thus reflect the average

nature of apportionments. The matching of these NMR-derived average distances with Monte Carlo and molecular dynamics simulations allows us to uncover these various apportionment scenarios. We invoked two separate strategies for distance measurements in the MTV-MOF system: 2D correlation experiments (3, 4) and rotational-echo double-resonance (REDOR) NMR (5–9). The former method enjoys broad applicability in polymer science (4), yet was inconclusive in the present study (10). The latter method proved to be decisive.

The REDOR NMR method provides a quantitative measure of distances between atoms. A pairwise measurement of the distance between two spectroscopically resolved nuclear spins and, hence, the corresponding atoms might seem an unlikely way to assess the apportionment of the functionalities of linkers because of the large number of possible linker configurations. The key to recovering apportionment of the functional groups from this measurement, however, is in how one

considers the averaging of point-to-point distances over the entire sample.

In the REDOR method, a period of multinuclear irradiation is incrementally increased so that the pairwise coupling between NMR-active isotopes evolves to yield "decay curves,". These curves are governed by the dipolar coupling constant between two spins (i and j), which is proportional to $1/r_{ij}^3$, where r_{ij} is their internuclear distance (11). We selectively labeled the spins at different linkers—for example, ^{13}C on linker X and ^{15}N on linker Y—to probe the intermolecular separation of these linkers. If the linkers are close, the average coupling is large and the decay is rapid; that is, a fast decay means that most of the linkers are in close proximity. Figure 2 provides a sketch of how these decay curves depend on the apportionment of functionalities for the different scenarios possible in MTV-MOF-5-BF. Indeed, faster decay is expected for the scenarios in the order of alternating, random, small, and large clusters (Fig. 2B).

To measure the REDOR curves, we ^{15}N labeled, in the case of MTV-MOF-5-BF, each amine group of linker B and measured its coupling to ^{13}C spins of the methyl groups [19 parts per million (ppm)]. Figure 2C shows the ^{13}C spectra measured in a $^{13}C\{^{15}N\}$ REDOR experiment at a given recoupling time with and without ^{15}N dipolar modulation, S and S_0, respectively. The S/S_0 ratio for the resonance at 19 ppm is plotted against a series of recoupling times to give S/S_0 decay data and shown in Fig. 3A. Similar data were obtained for MTV-MOF-5-EF, EI, and EHI and are overlaid on the predicted REDOR curves (Fig. 3A).

The apportionment can be derived from a model if we assume that linkers with different functional groups are predisposed to have different neighbor preferences and that we can express these preferences as effective interaction energies. A Monte Carlo simulation (12) is then conducted whereby linkers between metal sites are randomly exchanged in a simulated lattice structure; a new apportionment is accepted according to the energy difference between the new and old apportionment. In this way, the effective interaction energies

## Linkers with different functional groups in MTV-MOF-5 structures
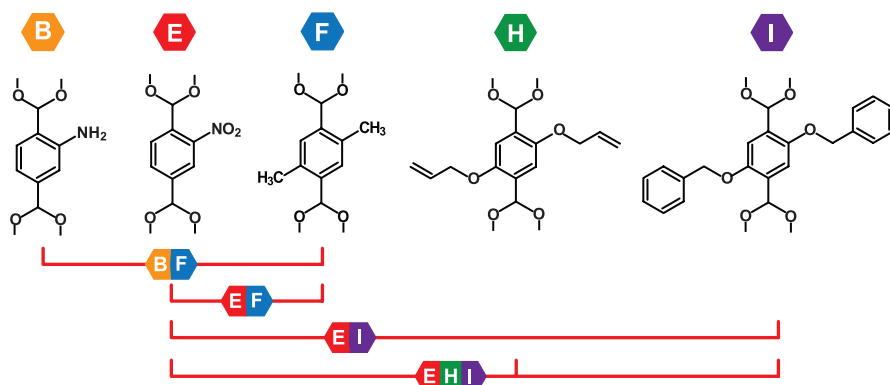
Fig. 1. MTV-MOF-5 linkers. Six linkers are combined with a Zn_4O "secondary building unit" to form an MTV-MOF-5. We use the linkers B, E, F, H, and I. Each linker has the same length but differs by their functional groups so that they can be interchanged to form a material with the same crystal lattice but different apportionment of the linkers. The amino and nitro groups on linker B and E, respectively, were 100% isotopically enriched with ^{15}N, whereas all other nuclei are present at natural isotopic abundance.
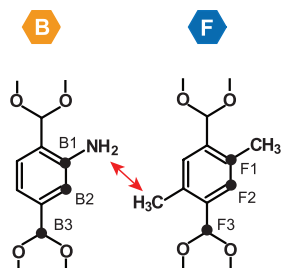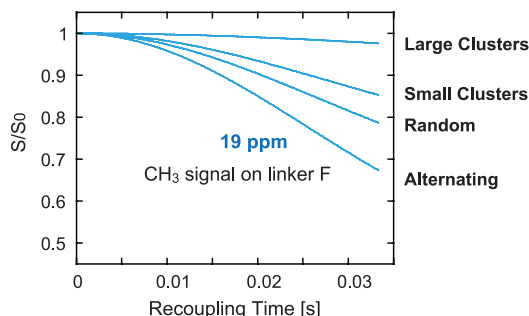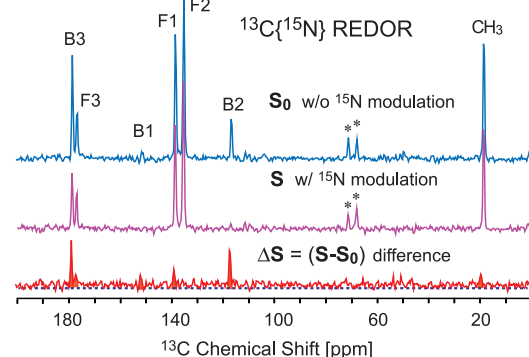

Fig. 2. Solid-state NMR results for MTV-MOF-5-BF. (**A**) The arrow represents the specific distance measured by our REDOR experiments. (**B**) Molecular dynamics simulations of the $^{13}C\{^{15}N\}$ REDOR S/S_0 decay curves for different BF apportionments. (**C**) A suite of ^{13}C spectra obtained from a $^{13}C\{^{15}N\}$ REDOR experiment at a given recoupling time. Blue, the ^{13}C spectrum taken without ^{15}N dipolar modulation, S_0; pink, the ^{13}C spectrum with ^{15}N dipolar modulation, S; red, the difference spectrum ΔS obtained by subtracting S from S_0. *, Spinning side bands.

determine the apportionment in a lattice model for which many configurations are generated using conventional Monte Carlo methods. The different apportionments lead to the distinct REDOR curves because these scenarios result in different average distances between atoms on different functional groups. In an alternating system, the majority of ^{13}C (on linker X)–^{15}N (on linker Y) are paired next to each other, and we observed fast decay. In a clustered system, the number of neighboring ^{13}C-^{15}N pairs is far less, and the REDOR S/S_0 decay is relatively flat. A quantitative measure of the REDOR curves was obtained by taking the apportionments of the functional groups from our lattice simulations and replacing the lattice model by the corresponding all-atom model. The subsequent molecular dynamics optimization provided the ensemble average of $1/r^3$ for all labeled pairs from which we computed the REDOR curves. Both the experiments and the simulation show that the decay was not sensitive to temperature. Figure 3B shows that for different materials, we could obtain a quantitative match with experimental data for the different apportionment scenarios, which yield materials that are visually quite different. For example, the EF linkers had a random distribution, the EI linkers were alternating, and clusters were formed for the BF linkers. To rationalize these results, we carried out density functional theory (DFT) calculations (10) to address the effect of functional group identity on the energy of formation of the metal-linker complex (table S3). Because of the electronegative -NO$_2$ group, the E linker has the least favorable energy of formation. This accounts for why we have been unable to synthesize a pure E MTV-MOF and why binary and ternary MTV-MOFs have a lower linker E content compared with their synthesis solution (table S1). The implication of these DFT calculations for apportionment is that the structural building units will minimize the number of E linkers, resulting in an apportionment biased toward an alternating structure. The B linker differentiates itself from others in that this linker can form hydrogen bonds both with other B linkers and with the synthesis solvent (13). One therefore would anticipate clustering in solution as an antecedent for the formation of clusters in the MTV-MOF.

With these apportionments, we can predict the adsorption properties of these materials. Figure 4 shows that the experimental isotherms of MTV-MOF-5-EI and EHI agree well with the ones derived from our best-fit models to the REDOR data and that alternative apportionments of large clusters fail to describe the adsorption isotherms. We can also use this result to rationalize the surprising enhancement of the selectivity for CO$_2$ over carbon monoxide (CO) observed in the MTV-MOF-5-EHI material compared with the single-linker MOF-5 material (2). The MOF-5 with E linkers lacks selectivity, while the ones with I linkers are too bulky and therefore block the pores. The combination of the two in an alternating functionality apportionment, however, creates the highly selective adsorption sites and sufficient pore space that are responsible
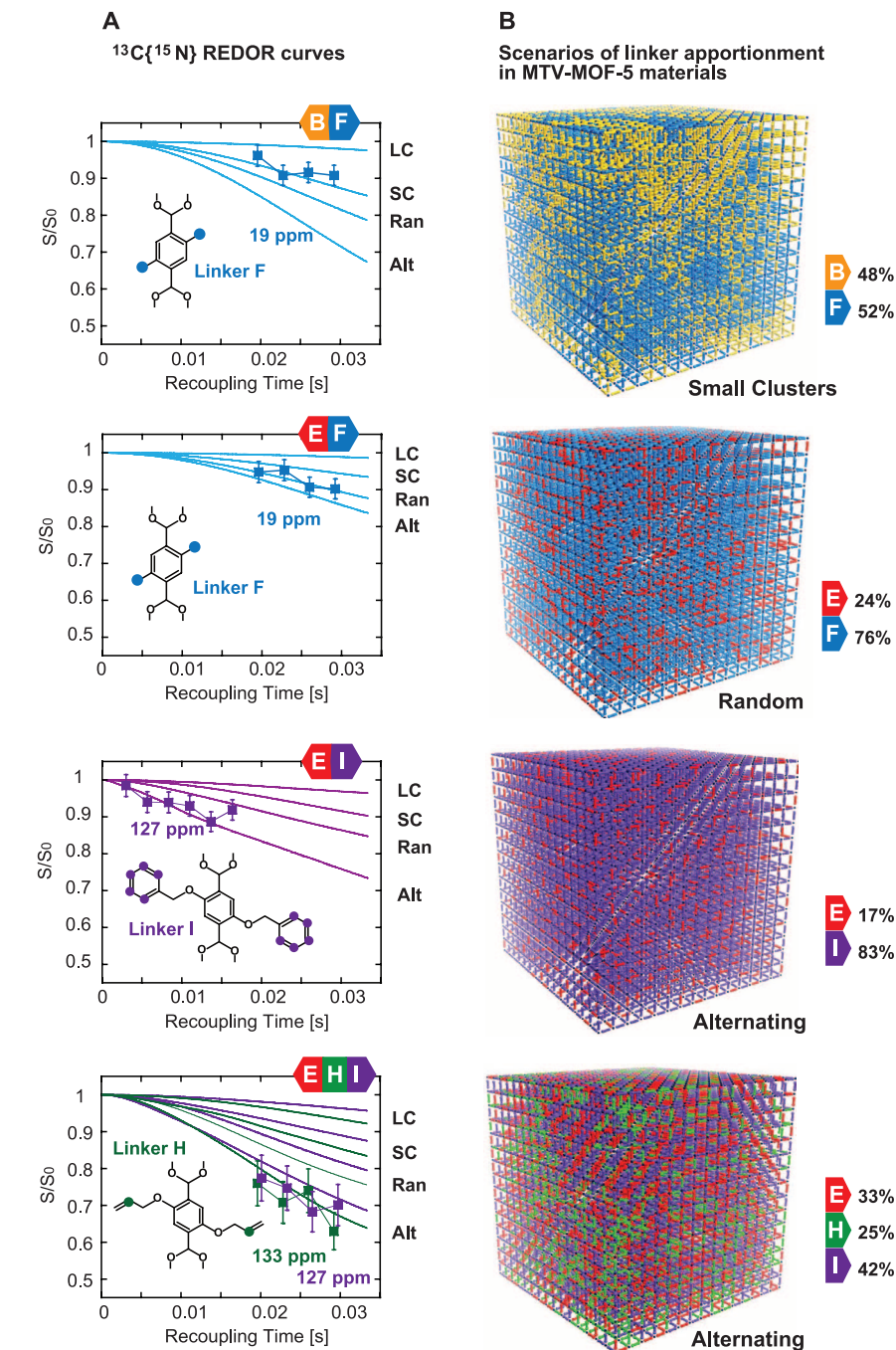

Fig. 3. REDOR results and apportionments. (**A**) Experimental ^{13}C{^{15}N} REDOR curves (squares) are compared with the molecular dynamics simulations for the different linker apportionments, large clusters (LC), small clusters (SC), random (Ran), and alternating (Alt). (**B**) The derived apportionments for the different MTV-MOF-5s. Yellow, linker B; blue, linker F; red, linker E; purple, linker I; green, linker H.

for the fourfold enhancement of the selectivity observed previously but unexplained (2).

Until now, we have used the effective interaction energies as fitting parameters for the NMR REDOR curves. We surmise that these effective energies describe the underlying interactions of the linkers during the formation of the MOF. We can use this model to predict the apportionment. For example, we successfully predicted the apportionments and corresponding REDOR curves

of compositions that were not yet synthesized (fig. S17). In addition, we predicted the effect of changes in the linker composition and the ternary linker apportionment on the basis of only binary interaction parameters (tables S6 and S7).

Our strategy to resolve apportionment in a disordered system consists of three parts: the synthesis of systems with disorder distributed upon an ordered lattice (in the present study MTV-MOFs); experimental measurement of pairwise
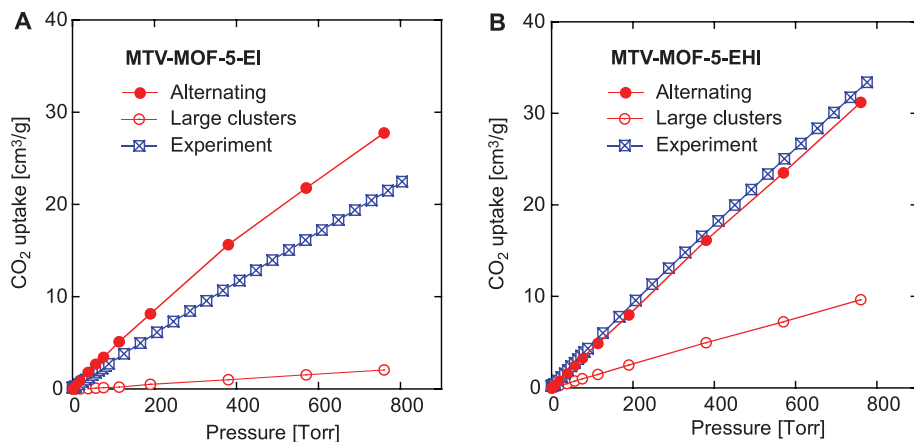
Fig. 4. CO$_2$ adsorption isotherms. (A) MTV-MOF-5-EI and **(B)** MTV-MOF-5-EHI. Experimental (blue) and simulated (red) at 298 K. Solid circles correspond to simulated isotherms for those linker apportionments that best fit the REDOR experiments. For reference, we have added simulation results for a large-cluster apportionment.

distances (here via NMR REDOR); and a computational method that allows us to directly simulate the disorder. This strategy may be employed for many issues in materials engineering, such as defect distributions in crystals and functional group distributions in block copolymers. It is our current vision to design and synthesize materials with crafted heterogeneity so as to carry out complex molecular operations such as recognizing, sorting, and counting substrates.

References and Notes
1. J. Hemminger et al., *From Quanta to the Continuum: Opportunities for Mesoscale Science* (U.S. Department of Energy, Washington, DC, 2012).
2. H. Deng et al., *Science* **327**, 846–850 (2010).
3. J. Jeener, B. H. Meier, P. Bachmann, R. R. Ernst, *J. Chem. Phys.* **71**, 4546–4553 (1979).
4. K. Schmidt-Rohr, H. W. Spiess, *Multidimensional Solid-State NMR and Polymers* (Academic Press, San Diego, CA, 1994).
5. T. Gullion, J. Schaefer, *J. Magn. Reson.* **81**, 196–200 (1989).
6. S. D. Cady et al., *Nature* **463**, 689–692 (2010).
7. L. Cegelski et al., *J. Am. Chem. Soc.* **132**, 16052–16057 (2010).
8. C. P. Jaroniec, B. A. Tounge, C. M. Rienstra, J. Herzfeld, R. G. Griffin, *J. Magn. Reson.* **146**, 132–139 (2000).
9. E. A. Louie, P. Chirakul, V. Raghunathan, S. T. Sigurdsson, G. P. Drobny, *J. Magn. Reson.* **178**, 11–24 (2006).
10. Materials and methods are available as supplementary materials on *Science* Online.
11. K. T. Mueller, *J. Magn. Reson. A* **113**, 81–93 (1995).
12. D. Frenkel, B. Smit, *Understanding Molecular Simulation from Algorithms to Applications* (Academic Press, San Diego, CA, 2002).
13. S. Loos, W. Seichter, E. Weber, F. Mertens, *Acta Crystallogr. Sect. E Struct. Rep. Online* **68**, o2501 (2012).

Microscopic Evidence for Liquid-Liquid Separation in Supersaturated CaCO$_3$ Solutions

Adam F. Wallace,[1,2,3]* Lester O. Hedges,[1,2] Alejandro Fernandez-Martinez,[1,4] Paolo Raiteri,[5] Julian D. Gale,[5] Glenn A. Waychunas,[1] Stephen Whitelam,[2] Jillian F. Banfield,[1,6] James J. De Yoreo[2,7,8]*

Recent experimental observations of the onset of calcium carbonate (CaCO$_3$) mineralization suggest the emergence of a population of clusters that are stable rather than unstable as predicted by classical nucleation theory. This study uses molecular dynamics simulations to probe the structure, dynamics, and energetics of hydrated CaCO$_3$ clusters and lattice gas simulations to explore the behavior of cluster populations before nucleation. Our results predict formation of a dense liquid phase through liquid-liquid separation within the concentration range in which clusters are observed. Coalescence and solidification of nanoscale droplets results in formation of a solid phase, the structure of which is consistent with amorphous CaCO$_3$. The presence of a liquid-liquid binodal enables a diverse set of experimental observations to be reconciled within the context of established phase-separation mechanisms.

Calcium carbonate (CaCO$_3$) has been intensely studied over the past century, and its most stable polymorph at ambient conditions, calcite, is often cited as a model of classical crystal growth behavior (1). However, findings from titration, ultracentrifugation (2, 3), and cryogenic transmission electron microscopy (cryo-TEM) (3, 4) now suggest that the onset of CaCO$_3$ mineralization—nucleation—contradicts classical expectations. In the classical picture, nucleation is a stochastic process in which thermal fluctuations induce the formation of clusters that are unstable with respect to dissolution. Clusters increase in both size and free energy until a threshold is crossed, whereupon the energy gained by forming the bulk material overcomes the penalty for creating an interface, and growth proceeds spontaneously. Contrasting with this classical picture, recent observations of long-lived nanometer-sized clusters present before nucleation have led to a predominant view of CaCO$_3$ formation in which the nucleation pathway is "nonclassical" (2, 3, 5–8), involving prenucleation clusters that are stable (or metastable) with respect to both dissolution and growth. In this model, bulk CaCO$_3$ forms primarily through aggregation of these clusters.

An alternative route to mineralization, liquid-liquid separation, has also been proposed based on light scattering, electron microscopy, and nuclear magnetic resonance (NMR) (9–11). This hypothesis is supported by experimental work documenting the formation of liquid magnesium sulfate (MgSO$_4$) at high temperature (12), as well as the known persistence of a polymer-stabilized liquid

[1]Earth Sciences Division, Lawrence Berkeley National Laboratory, Berkeley, CA 94720, USA. [2]The Molecular Foundry, Lawrence Berkeley National Laboratory, Berkeley, CA 94720, USA. [3]Department of Geological Sciences, University of Delaware, Newark, DE 19716, USA. [4]Institut des Sciences de la Terre (ISTerre), Université de Grenoble 1, CNRS, 38041 Grenoble, France. [5]Nanochemistry Research Institute, Department of Chemistry, Curtin University, Post Office Box U1987, Perth, WA 6845, Australia. [6]Department of Earth and Planetary Science, University of California, Berkeley, Berkeley, CA 94720, USA. [7]Materials Sciences Division, Lawrence Berkeley National Laboratory, Berkeley, CA 94720, USA. [8]Physical Sciences Division, Pacific Northwest National Laboratory, Richland, WA 99352, USA.

*Corresponding author. E-mail: afw@udel.edu (A.F.W.); james.deyoreo@pnnl.gov (J.J.D.Y.)